

Geometric Shape Recognition with an Ultra-High Density Perovskite Nanowire Array-Based Artificial Vision System

Swapnadeep Poddar,[†] Zhesi Chen,[†] Shivam Kumar, Daquan Zhang, Yucheng Ding, Zhenghao Long, Zichao Ma, Qianpeng Zhang, and Zhiyong Fan*



Cite This: <https://doi.org/10.1021/acsami.3c18719>



Read Online

ACCESS |



Metrics & More



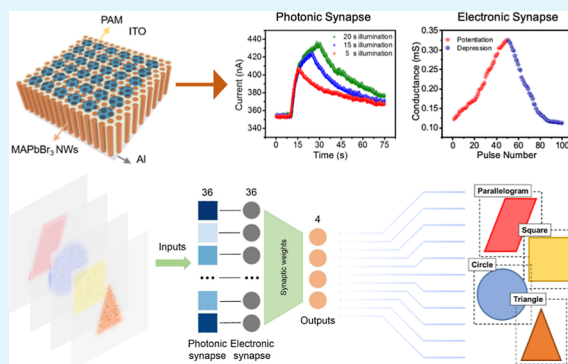
Article Recommendations



Supporting Information

ABSTRACT: Artificial vision systems (AVS) have potential applications in visual prosthetics and artificially intelligent robotics, and they require a preprocessor and a processor to mimic human vision. Halide perovskite (HP) is a promising preprocessor and processor due to its excellent photoresponse, ubiquitous charge migration pathways, and innate hysteresis. However, the material instability associated with HP thin films hinders their utilization in physical AVSs. Herein, we have developed ultrahigh-density arrays of robust HP nanowires (NWs) rooted in a porous alumina membrane (PAM) as the active layer for an AVS. The NW devices exhibit gradual photocurrent change, responding to changes in light pulse duration, intensity, and number, and allow contrast enhancement of visual inputs with a device lifetime of over 5 months. The NW-based processor possesses temporally stable conductance states with retention $>10^5$ s and jitter $<10\%$. The physical AVS demonstrated 100% accuracy in recognizing different shapes, establishing HP as a reliable material for neuromorphic vision systems.

KEYWORDS: halide perovskite, nanowires, artificial synapses, artificial vision system, shape recognition



INTRODUCTION

Human beings perceive the majority of information from the external environment via their sense of vision. The vision pathway in humans specifically comprises a retina, optic nerves, and the visual cortex in the brain. The retina consists of photoreceptors, bipolar, and ganglion cells, which perform image sensing, neural stimulation, and preprocessing of the perceived image, respectively. The optical nerves transfer the sensed signals to the visual cortex where memorization, processing, and computing take place.^{1,2} To replicate the integration of visual sensing, preprocessing, information relay, processing, and memorization, neuromorphic vision systems have come to the fore. Such systems show potential in various applications in visual prosthetics and artificially intelligent robotics.^{3,4} Physical artificial vision systems explicitly comprise two layers in order to effectively mimic a human vision system. The first layer is predominantly an artificial photonic synapse that senses the visual information and performs image preprocessing and image memorization to a certain extent. The second layer is usually an electronic artificial synapse, made of nonvolatile memories like resistive random access memories (Re-RAMs), which can perform processing and computing tasks of recognition and classification upon training with machine learning algorithms and can also store the perceived visual information.^{5,6}

Owing to their tunable bandgap, long charge diffusion length, high absorption coefficient, and high color purity, halide perovskites (HPs) have garnered tremendous scientific interest in the fields of optoelectronics and photovoltaics.^{7–14} In conjunction with the excellent optical traits, HPs also possess ion migration pathways, hysteresis, and defect states in abundance, which facilitate the trapping and detrapping of photogenerated charges and have thus been vehemently used recently in developing photonic synapses.^{15–20} However, thin-film-based perovskites suffer from instability and variability issues, which limit their applicability in artificial vision systems.²¹ Specifically, to date, the literature has only reported perovskite-based artificial vision systems comprising the first photonic synaptic layer, and the second layer is always simulated instead of being a physical device that can compute, process, and store the preprocessed optical information. Herein, we developed an artificial vision system with ultrahigh-density vertically assembled perovskite NWs in the porous alumina membrane (PAM) as the photosynaptic as

Received: December 14, 2023

Revised: December 22, 2023

Accepted: December 22, 2023

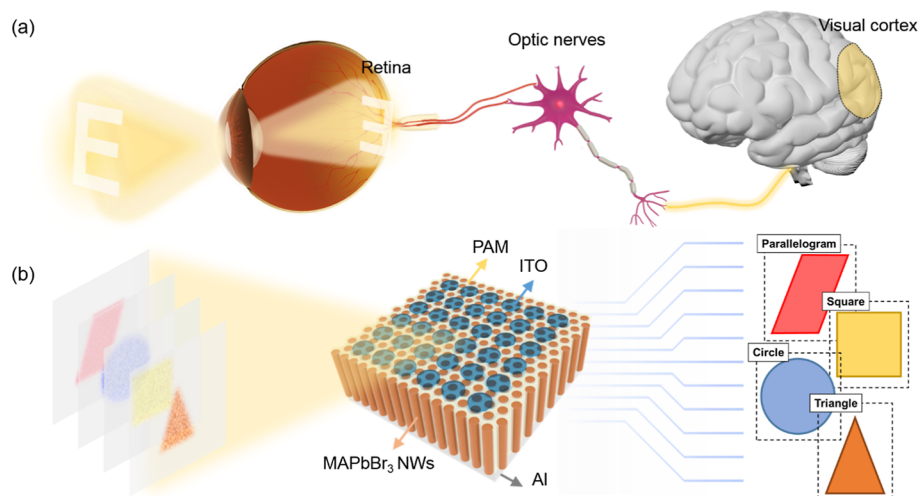


Figure 1. Schematic illustration of biological and artificial vision systems. (a) Illustration of the biological vision system comprising the retina, optic nerves, and the visual cortex. (b) Illustration of the MAPbBr₃ NW-based neuromorphic vision system performing preprocessing and discrimination of geometric shapes, emulating the biological vision system.

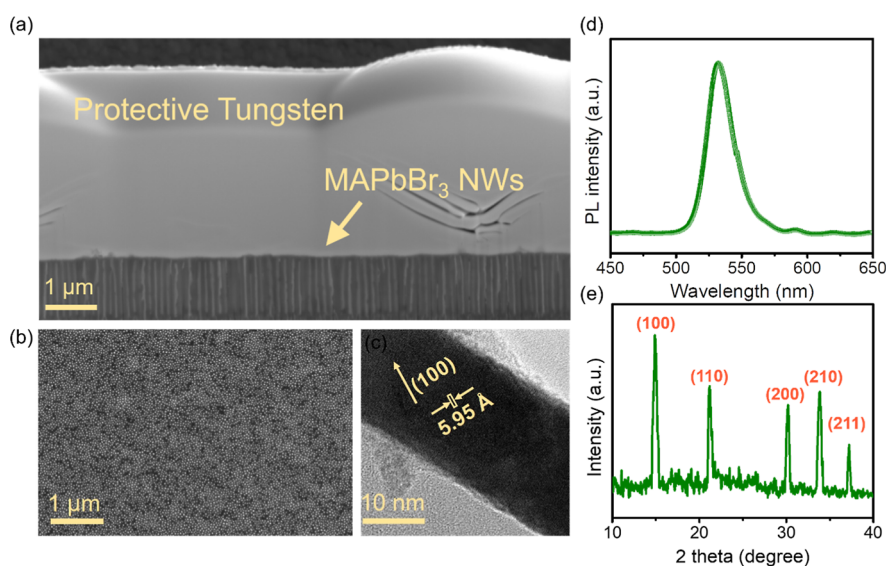


Figure 2. Morphological and material study of the MAPbBr₃ NWs. (a) Cross-sectional SEM image of the MAPbBr₃ NWs (30–40 nm diameter and 1–1.5 μm length) embedded in the PAM. A protective tungsten layer was used to prevent damage to the delicate perovskite during the focused-ion-beam cut. (b) Top-view SEM image of the MAPbBr₃ NWs in the PAM exhibiting ultrahigh NW density. (c) HRTEM of MAPbBr₃ NW exhibiting single crystallinity and the presence of the (100) crystal plane. (d) Photoluminescence spectrum of the MAPbBr₃ NWs in the PAM. (e) XRD spectrum of the MAPbBr₃ NWs in the PAM.

well as the processing layer with superlative stability and performance metrics compared to their thin-film counterparts. The methylammonium lead bromide (MAPbBr₃) NWs in the PAM exhibited enhancement in photosynaptic current with an increase of intensity as well as the duration of light stimuli, apart from exhibiting light-induced paired-pulse facilitation (PPF), thereby substantiating their mettle in the preprocessing of perceived visual information. The NWs further exhibited potentiation–depression, stable long-term potentiation (LTP) states with retention >10⁵ s and temporal jitter <10%, demonstrating its potential in processing and computing. Finally, an artificial vision system was developed in the form of a 6 × 6 array, which performed preprocessing in the form of contrast enhancement and subsequent processing in the form of accurate recognition of geometrical shapes. The artificial vision system developed in this work opens up new avenues for

utilizing high-performance nanostructured perovskite for various applications in machine intelligence, pattern recognition, and brain-inspired computing.

RESULTS AND DISCUSSION

Concept Flow and Illustration of the Artificial Vision System. The concept flow of the study is presented in Figure 1. Figure 1a illustrates the biological vision system comprising the retina perceiving the input visual information, the optical neuron-synapse interconnects performing the preprocessing and information relay, and finally, the visual cortex performing the processing and storage tasks. Figure 1b shows the MAPbBr₃ NW Re-RAM device emulating the biological vision system, receiving visual inputs in terms of multiple overlapping, noisy geometrical shapes, and subsequently performing contrast enhancement and shape recognition.

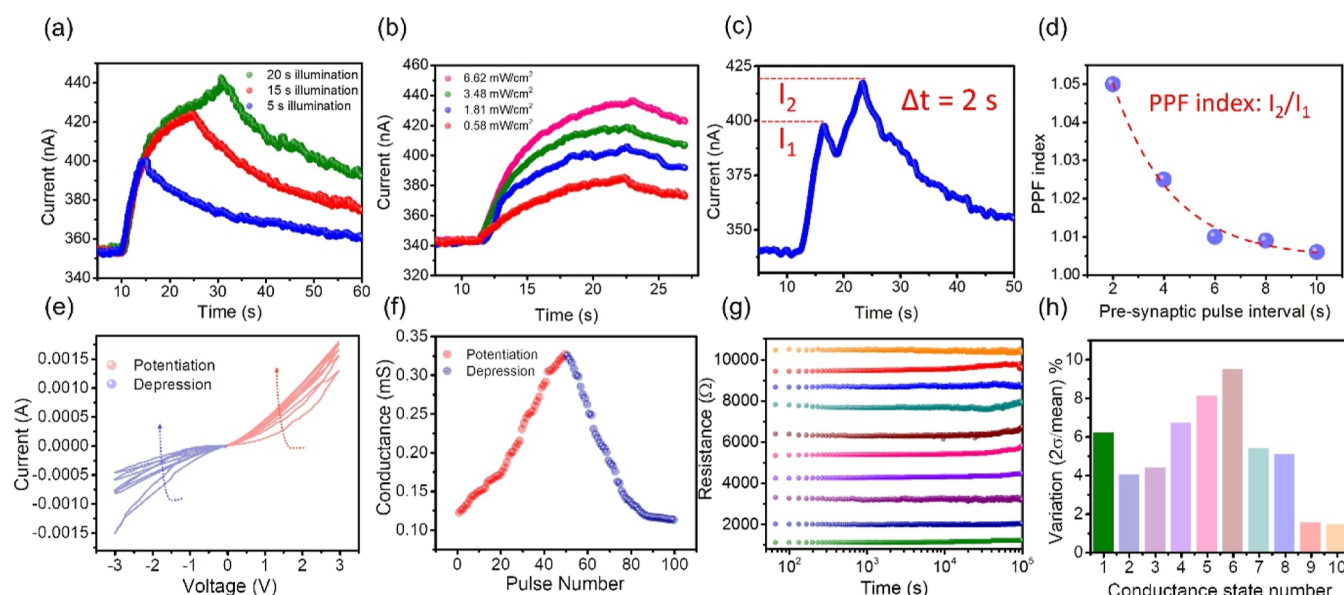


Figure 3. Synaptic behavior in MAPbBr₃ NW-based Re-RAM. (a) Plot showing enhancement of current in the MAPbBr₃ NW-based photonic synapse upon varying illumination time at a fixed intensity. (b) Plot showing enhancement of current in the MAPbBr₃ NW-based photonic synapse upon varying illumination intensity for a fixed illumination time. (c) Current response in the MAPbBr₃ NW-based photonic synapse upon illumination by paired presynaptic light pulses. $\Delta t = 2$ s is the time interval between the end of the first light pulse and the beginning of the second. (d) Plot showing paired pulse facilitation (PPF) with varying light pulse intervals in the MAPbBr₃ NW-based photonic synapse, corresponding to the current response as typically shown in (c). (e) Plot showing I – V characteristics of the MAPbBr₃ NW-based electronic synapse. (f) Plot showing potentiation–depression characteristics of the MAPbBr₃ NW-based electronic synapse. A reading voltage of 0.1 V is used for the test. It is to be noted that 0.1 V was also used for the LTP retention test of the thin-film sample shown in Figure S3a. (g) Plot showing retention of the LTP conduction states in the MAPbBr₃ NW-based electronic synapse. A reading voltage of 0.1 V is used for the test. It is to be noted that 0.1 V was also used for the LTP retention test of the thin-film sample shown in Figure S3a. (h) Plot showing jitter of the LTP conduction states in the MAPbBr₃ NW-based electronic synapse.

Structural and Material Reliability Study of MAPbBr₃ NWs. Figure 2a shows the cross-sectional scanning electron microscopy (SEM) image of MAPbBr₃ NWs embedded in the PAM substrate. A protective tungsten layer was deposited on top of the NWs to prevent damage to the electron- and ion-beam-sensitive perovskite material while cutting a lamina using the focused ion beam technique. Figure 2b shows the top-view SEM image of the NWs in the PAM, demonstrating a 90–100% fill ratio and an ultrahigh density of $\sim 10^{10}$ cm⁻². Figure 2c shows a high-resolution transmission microscopy (HRTEM) image of the single-crystalline NW with the dominant (100) lattice plane. Figure 2e,f, respectively, show the photoluminescence (PL) spectrum having a peak at ~ 530 nm and the X-ray diffraction (XRD) spectrum of the NWs demonstrating excellent material and crystal quality. The single crystalline NWs are grown by a vapor–solid–solid-reaction process (see Materials and Methods section).⁹ In this context, it must also be mentioned here that the PAM instills mechanical and electrical robustness in the NWs. HP NWs offer significant advantages over thin-film perovskites in the field of photonic synapse-aided artificial vision systems. These nanowires (NWs), enclosed in a PAM layer, possess improved material and electrical stability, resulting in reliable photosynaptic behavior and stable conduction states. The reduced number of surface diffusion pathways in PAM-aided NWs significantly reduces moisture-induced attacks, enhancing material stability. The high thermal conductivity of the PAM walls aids in proper heat dissipation, uplifting thermal stability. The insulating PAM walls prevent lateral cross-talk between adjacent NWs and pixels, improving the overall electrical stability. Additionally, the strictly single-crystalline nature of the NWs allows for more facile movement of ions and charges

compared to polycrystalline thin films. Thus, the performance metrics of the NWs are elevated to the state-of-the-art compared to their thin film counterparts.^{9,22–25} Results demonstrating better material reliability under ambient conditions in the NWs in comparison to the thin-films have been shown in Supporting Information Figure S1. Specifically, the unpackaged NWs, without any NOA81 epoxy-based top-surface passivation, showed intact PL and XRD spectra even after 7 days of exposure to a 50–60% relative humidity environment, whereas the material integrity of the unpackaged thin-film counterpart withered away after 7 days.

Synaptic Behavior of MAPbBr₃ NW-Based Re-RAMs.

Figure 3a–d shows the photonic synapse behavior of the perovskite NW devices. Figure 3a shows the impact of the duration of the light stimuli on synaptic behavior. Keeping the intensity fixed to 3.48 mW/cm², the duration of the stimulus is varied from 5 to 20 s. It is observed that the longer is the duration of the stimulus, the higher is the post synaptic current and the stronger is the established synaptic connection. Similarly, keeping the duration fixed at 10 s, the intensity is varied from 0.06 to 6.62 mW/cm². As seen from Figure 3b, the stronger is the input intensity of light, the higher is the postsynaptic current. The optical paired pulse facilitation (PPF) test was carried out on the devices where the ratio of the current obtained from the second optical pulse to the current obtained from the first optical pulse was monitored versus the interval between the two pulses, as shown in Figure 3c,d. It is observed that the smaller is the interval, the higher is the PPF index. A small bias voltage of 0.5 V is applied to the devices during photonic synapse characterization. In order to evaluate the long-term performance or lifetime of the MAPbBr₃ NW devices, the photonic synaptic behavior is

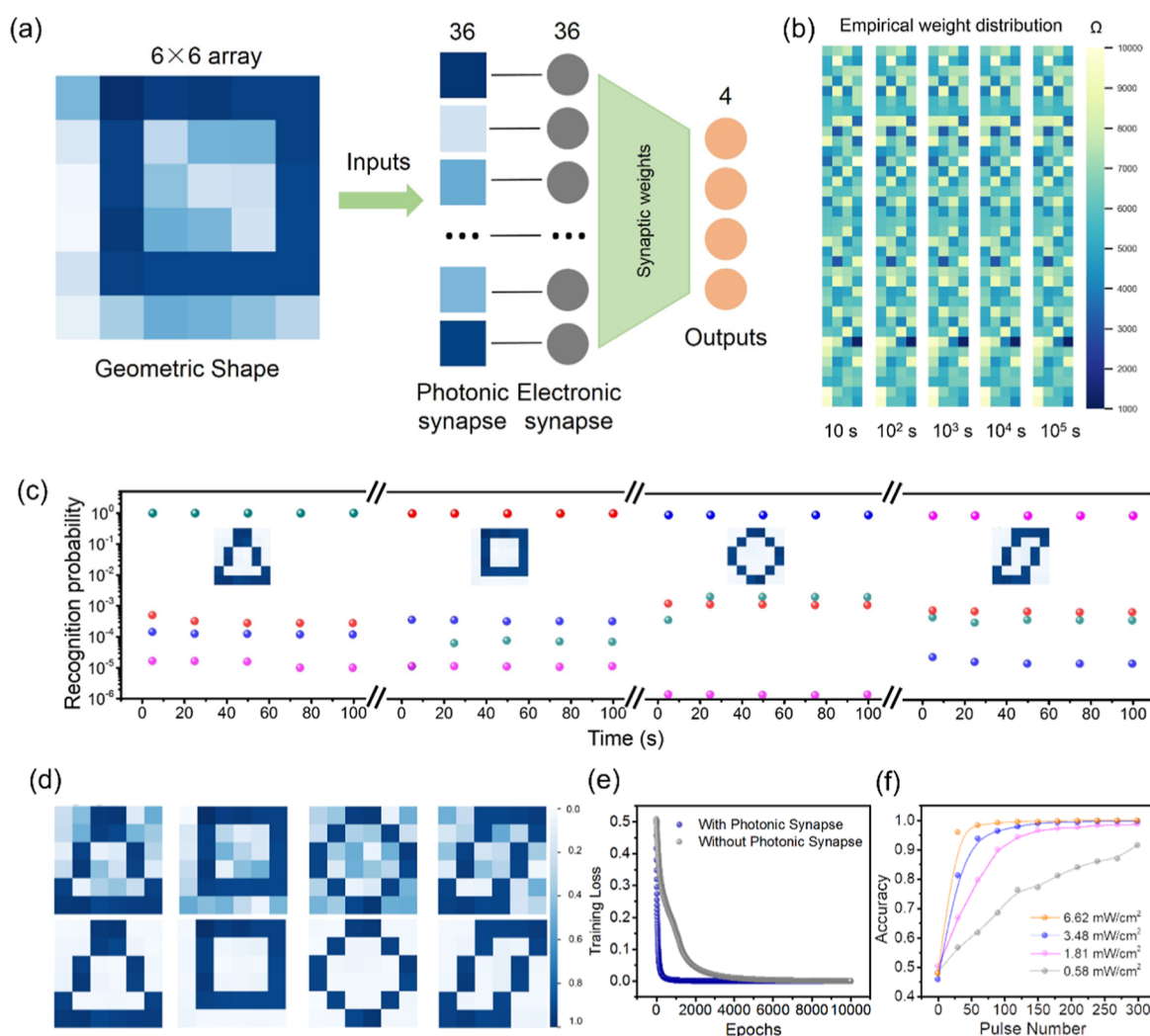


Figure 4. Geometric shape recognition with a MAPbBr₃ NW-based artificial visual system. (a) Illustration showing the “square” shape as input to the MAPbBr₃ NW artificial synapse-based neural network. (b) Matrix plot showing the distribution and retention of resistances or weights in the 6 × 6 MAPbBr₃ NW artificial synapse-based neural network. (c) Plot showing the recognition of the geometric shapes as performed by the 6 × 6 MAPbBr₃ NW artificial synapse-based neural network. (d) Plot showing the comparison of classification results for training images with (top row) and without randomly generated noise (bottom row). (e) Plot showing the training loss convergence for with and without the photonic synapse layer. (f) Plot showing the accuracy of shape recognition with varying intensities of incident light.

traced for 5 months without any sign of performance degradation, as shown in Supporting Information Figure S2. To demonstrate the electronic artificial synaptic behavior, current–voltage (I – V) sweeps are performed on the MAPbBr₃ NW devices, as shown in Figure 3e. During the subsequent positive sweeps (0 V → 3 V → 0 V), the device showed an enhancement in conductance, exhibiting the synaptic potentiation trait. The device in high conductance state is then subjected to repeated negative sweeps (0 V → –3 V → 0 V), and a gradual reduction in a conductance is observed, exhibiting the depression behavior. The pulse-based potentiation–depression tests are also carried out, as shown in Figure 3f. A gradual rise in device conductance is observed with a pulse scheme of +5 V, 10 ms (write)/0.1 V, and 10 ms (read), and a gradual drop is observed with a pulse scheme of –5 V, 10 ms (write)/0.1 V, and 10 ms (read), bolstering the I – V sweep result. The pulse-based test was used to generate temporally robust and stable LTP conduction states by varying the pulse number, as shown in Figure 3g,h. The LTP states could be retained for >10⁵ s with a jitter or temporal variation

($2\sigma/\text{mean}$) < 10%, in stark contrast to the thin-film counterpart, which could produce LTP states with a duration of ~16,000 s and jitter ~25 to 70% (see Figure S3). The overall performance enhancement is attributed to the excellent electrical and material stability of the perovskite NWs in the PAM encapsulation, which is absent in the thin films.

The artificial synaptic behavior upon exposure to optoelectronic/electronic stimuli in halide perovskite is typically ascribed to the interfacial defect states, which allow gradual trapping and detrapping of carriers. The interfacial traps and defects can act as nucleation sites for the formation of conductive filaments, which are chains of charge carriers facilitating device conduction.^{15,21,26,27} As shown in Supporting Information Figure S4, when the top ITO electrode was replaced by a semitransparent gold (Au) electrode, the photosynaptic behavior vanished and instead a standard photodetector behavior was observed, devoid of any gradual enhancement and the reduction of device conductance under illumination and in the dark, respectively. The result clearly indicates that the ITO/HP NW interface is crucial for the

exhibition of the synaptic trait. For the device architecture described herein, the gradual modulation of device conductance is ascribed to the plausible trapping and release of charges at the defects near the ITO/HP NW interface.^{28,29} Overall, the excellent photonic and electronic synaptic behavior demonstrated by the NW device paves the way for its utilization in artificial vision systems.

Implementation of the MAPbBr₃ NW-Based Artificial Vision System. We built the artificial vision system combining the photonic synapse layer and Re-RAM-based processing layer, where signal perception, data storage, and processing are achieved, with the device architecture remaining the same for both layers. As illustrated in Figure 4a, the architecture of the artificial visual system consists of the perception layer (36), an input layer (36), and an output layer (4). The final neuronal output is calculated with a nonlinear activation function as below

$$\text{output} = \text{sigmoid}(\sum_{i=0}^{36}(\text{pixel}_i \times \text{weight}_i))$$

where i represents each pixel of input images detected by the photonic synapse, and weight is the neural weight of the neural network, obtained by online training of the artificial vision system.

At the onset, we transfer the online-trained weights to the Re-RAM-based processing layer.³⁰ The specific distribution of weights across the Re-RAM devices is plotted in Figure 4b. It is also clearly observed that the weights remain constant over a period of 10^5 s, which provides more than enough time for completely achieving the processing task. The four sets of resistance values represent the weights corresponding to four different geometric shapes. The visual information on images is first obtained and preprocessed by the photonic synapse layer, in which the noise is suppressed and contrast is enhanced, akin to the human retina. Next, mimicking the function of the visual cortex, the preprocessed visual images are expanded to one column and further flow through the Re-RAM processing layer, which detects and extracts the patterns existing in the images. Through the process above, the shape or pattern of the input images is classified accordingly. See Figure S5 for a process flow depicting the processing task.

Figure 4c depicts the recognition probability of each shape. For each shape: triangle, square, circle, and parallelogram, our artificial vision system can state with more than 99.9% confidence the right category of the shapes, while the probabilities of false shapes are as close as 0% with limited variation (much smaller than 0.1%) at different times.

To check the robustness and efficacy of our artificial vision system, we compare the classification results with and without noise data sets, as shown in Figure 4d,e. The background noise in each image is randomly generated in the range of 0–0.5, as displayed in Figure 4d. As shown in Figure 4e, with the photonic synapse as the preprocessing layer, the training loss of the artificial neural model converges faster than the one without the photonic synapse layer. Also, the recognition accuracy with the photonic synapse layer reaches 100% after 66 training epochs, while without this layer it takes around 2348 epochs, as illustrated in Figure S6. This comparison shows that the training speed of the model is greatly improved with the incorporation of the photonic synapse as the preprocessing layer.

It is also important to gauge the efficacy of the artificial vision system in an environment with variable light intensity and variable light pulse number; hence, we vary the intensity of

input light stimuli over 0.50, 1.81, 3.48, and 6.62 mW/cm².³¹ Supporting Information Figure S7 shows the variation in the postsynaptic photocurrent by altering the intensity and number of light pulses for a single MAPbBr₃ NW-based photonic synapse device. By using different light intensities and varying light pulse numbers, the postsynaptic photocurrent gradually changes in the range of 349 and 500 nA. A geometric shape depicting a “square” is perceived under different light intensities and pulse numbers by the MAPbBr₃ NW-based 6 × 6 photonic synapse array, as shown in Figure S8. With higher light intensity and an increased pulse number, the image of the detected square becomes clearer with significantly better contrast. Figure 4f shows the impact of the incorporation of various light intensities on the recognition accuracy. When the input light intensity is only 0.58 mW/cm², the classification confidence can reach 91.5%, while with an increase of both input light intensity and pulse number, the classification confidence quickly reaches 99.9% with an input light intensity of 6.62 mW/cm² as the light pulse number is varied until 300. The results clearly indicate that the MAPbBr₃ NW-based artificial vision system has the ability to accurately recognize patterns or images under variable light intensities.

CONCLUSIONS

Artificial vision systems consist of a preprocessor, which is a photonic synapse that preprocesses input images, and a processor that computes and processes the preprocessed data with high accuracy. However, until now, halide perovskite thin film-based artificial vision systems have only possessed a physical preprocessor, with the processor's task being mostly simulated. This is due to the weak and jittery conduction states that hinder the systematic tuning of the artificial synaptic weights or resistances. In this study, a perovskite-based artificial vision system has been reported for the first time that combines a physical processor with a physical preprocessor. This breakthrough was made possible by improving the material and electrical stability of the PAM-enclosed NWs, resulting in reliable photosynaptic behavior and stable and temporally robust conduction states. The NWs embedded in a PAM produced a superlative performance in terms of retention and jitter of the conduction states and better material reliability when compared to their thin-film counterpart, enabling the building of a physical artificial vision system. Specifically, the devices show retention $>10^5$ s and temporal jitter $<10\%$. The MAPbBr₃ NW devices also exhibit photosynaptic behavior by responding to changes in intensity, duration, and number of light pulses, consequently enabling the device to perform contrast enhancement, aka preprocessing of perceived visual information, with a device lifetime of over 5 months. Finally, a 6 × 6 array of MAPbBr₃ NW devices is utilized in realizing a physical artificial vision system which can preprocess and successfully recognize four different geometric shapes. The artificial vision system demonstrated in this work elevates HP as a state-of-the-art and reliable active layer, enabling a plethora of applications in artificial intelligence mimicking the human vision system. Furthermore, in the future, using ultrahigh-density HP NWs, a larger-scale artificial vision-based neural network can be realized with compact and monolithic integration of the preprocessing and processing layers.

MATERIALS AND METHODS

Materials. Methyl ammonium bromide (MABr) powder was obtained from DYESOL.

Device Fabrication. PAM Fabrication. The porous alumina membranes (PAMs) were fabricated using a two-step anodization process of high-purity aluminum (Al) foils, as previously reported. Initially, Al foils with a thickness of 0.25 mm were cut into 2.5×2 cm pieces and subjected to a rigorous cleaning process involving acetone and isopropyl alcohol. Subsequently, the sheets were electrochemically polished in an acidic solution consisting of 25 vol % perchloric acid (HClO_4) mixed with 75 vol % absolute ethanol ($\text{CH}_3\text{CH}_2\text{OH}$) for 5 min under a 19 V potential at 10 °C. The polished Al substrates were then immersed in a solution of oxalic acid ($\text{H}_2\text{C}_2\text{O}_4$) at a concentration of 0.2 M by volume for anodization. An anodization voltage of 40 V was applied, and the process was carried out at a temperature of 10 °C for 10 min. Following the first anodization, the oxide layer was etched away in a mixture of phosphoric acid (H_3PO_4) and chromium trioxide (CrO_3) at a concentration of 6 and 1.8 wt %, respectively, at a temperature of 98 °C for 10 min. Subsequently, a second anodization was carried out under the same conditions for 20 min to obtain a PAM with a thickness of approximately 1 μm . This process resulted in the creation of a highly ordered, hexagonally arranged nanoporous structure with uniform pore size, which is ideal for the growth of NWs.

Barrier Thinning and Pb Electrodeposition. In order to enable the electrochemical deposition of lead (Pb) nanoclusters within the nanoporous structure of PAMs, a voltage-ramping-down process was implemented to thin the barrier layer at the bottom of the nanochannels. This process involved an additional step carried out in a 0.2 M oxalic acid solution at room temperature, which was computer-controlled using a Keithley 2400 instrument. Initially, the Keithley 2400 was set to voltage-source mode, and the anodization voltage was gradually increased to 50 V while the electric current (I_0) was recorded. Subsequently, the Keithley 2400 was switched to current-source mode, and the current was set to $I_0/2$, resulting in a gradual decrease in current. Once the current declining rate slowed to less than 3 V min^{-1} , the voltage measured was approximately 25 V. The current was then adjusted to $I_0/4$ to expedite the voltage-declining process, and when the voltage reached 4 V, the process was terminated. The entire process took approximately 10 min. Following barrier thinning, Pb was electrochemically deposited at the bottom of the PAM channels in a three-electrode system by using an alternating-current method with a potentiostat (SG 300, Gamry Instruments). The electrolyte was prepared by dissolving 1.7 g of lead(II) chloride (PbCl_2) and 25 g of trisodium citrate ($\text{Na}_3\text{C}_6\text{H}_5\text{O}_7$) in 100 mL of water with continuous stirring. A 60 Hz sinusoidal voltage was applied for 10 min, and the amplitude was adjusted from 3 to 9 V to maintain a peak current density of 2 mA cm^{-2} during the negative deposition cycle. Following deposition, the chip was rinsed several times with deionized water to remove any adsorbed chemicals.

VSSR Growth of MAPbBr_3 NWs. The growth of methylammonium lead bromide (MAPbBr_3) NWs involved a vapor–solid–solid-reaction (VSSR) process between methylammonium bromide ($\text{CH}_3\text{NH}_3\text{Br}$) powder and electrodeposited Pb at 185 °C and 350 standard cubic centimeters per minute (sccm) continuous argon flow within the confines of the PAM walls. A residual thin film of perovskite atop the PAM was carefully removed by a lose-dose ion-milling process (100 V for 1 h with the stage tilted at 85° w.r.t. the bombarding ions to suppress damage to the exposed NWs). Following the ion-milling process, a short regrowth of the NWs was carried out by the before-mentioned VSSR technique for 2 min. This process created highly crystalline NWs with a uniform diameter and high aspect ratio that are ideal for use in electronic and optoelectronic devices.

Depositing Electrodes and Packaging of the Device. The deposition of electrodes involved using radiofrequency (RF) sputtering to deposit indium tin oxide (ITO) electrodes (100 nm thick) on top of NWs using metal shadow masks with a 4 mm^2 area and 2 mm spacing between each electrode. The sputtering process

used a power of 200 W and a pressure of approximately 0.30 Pa to create a uniform layer of ITO. The devices were then packaged using NOA81 ultraviolet (UV) curable epoxy, which provided protection against environmental factors and ensured the stability of the device. The curing was carried out for 20 min.

Control Sample Fabrication. For the control test sample, a semitransparent gold (Au) layer of thickness 10 nm was deposited on top of the NWs in the PAM after the regrowth process by the thermal evaporation technique at a pressure of 5×10^{-4} Pa and an evaporation rate of 0.1 nm per second. On top of the Au contact, a 90 nm layer of ITO was RF sputtered.

Thin Film Sample Fabrication. For the thin-film sample, a precursor solution was prepared by dissolving $\text{CH}_3\text{NH}_3\text{Br}$ and lead bromide (PbBr_2) in N,N' -dimethylformamide (0.5 g/mL) and dimethyl sulfoxide (DMSO) (1.1 g/mL). The solution was then spin-coated onto an electropolished planar aluminum substrate devoid of any PAM. To assist in the crystallization process of MAPbBr_3 , the coated chips were annealed at 110 °C for 20 min. ITO electrodes (100 nm thick) were then deposited as the top electrode via a radio frequency (RF) sputtering process using a shadow mask to create separate pixels. The electrode spacing was 2 mm between two separate pixels, and the device area was 4 mm^2 , which allowed for the measurement of the properties of the thin-film sample.

The overall device fabrication has been schematically illustrated in Supporting Information Figure S9.

Morphological and Structural Characterization. The lamella for SEM imaging was made using a dual-beam FIB/FESEM system called FEI Helios G4 UX, and FESEM was used to view the cross-section. This system has a Ga⁺ ion beam and a high-resolution scanning electron column that can work together. The high crystallinity of the NWs was studied using a transmission electron microscope called JEM 2010 (JEOL) and a D8 X-ray diffractometer. The PL emission spectrum was obtained from the FLS920P fluorescence spectrometer.

Electrical Characterization. Single-Device Measurements. The single pixel measurement corresponding to Figure 3a–d in the manuscript was performed with a probe-station embedded halogen source lamp (wavelength range: 300–650 nm) with tunable intensity capability and a reading voltage source in the form of a Keithley 4200 SCS's SMU unit. Specifically, the light was focused on the device (mounted on the probe station on a vacuum stage), and the photocurrent was read by the Keithley 4200 SCS. The positive voltage was applied to the top ITO electrode, and the bottom Al electrode was grounded.

The single-pixel measurement corresponding to Figure 3e–h was performed jointly by the Keithley 4225 PMU Ultrafast IV module and the 4200 SCS. The I – V curves in Figure 3e were traced with the Keithley 4200 SCS's SMU. The potentiation–depression measurement corresponding to Figure 3f was performed with the Keithley 4225 PMU Ultrafast IV module's arbitrary waveform generator for producing the write/read and erase/read pulse sequences. The resistances corresponding to Figure 3g were measured with the “two-wire resistance” mode of the Keithley 4200 SCS, which supplied a small continuous readout voltage of 0.1 V. During all the single-pixel electrical measurements, the positive voltage was applied to the top ITO electrode, and the bottom Al electrode was grounded.

Array Measurements. The array measurements corresponding to Figure 4 were performed with a custom homemade system including a Keithley 2450 source meter, a PXI2530B National Instruments multiplexer, a PXI4130 National Instruments volt-meter installed in a PXI1031 National Instrument chassis box, a Keithley 6487 preamplifier, a convex lens, and custom-made LABVIEW programs.

Photonic Synapse Array. The geometric patterns generated by PowerPoint slides emanating from the projector were projected onto the 6×6 MAPbBr_3 NW photonic synapse device via a convex lens intended for focusing the image. The Keithley 2450 source meter was used to supply a voltage of 0.5 V. The device output was passed through the preamplifier and then read with the voltmeter. The multiplexer is used for device selection, and the whole system was controlled via LABVIEW programs. The device was placed inside a

metal box to reduce the overall measurement noise. See Figure S10a of Supporting Information for a schematic illustration.

Electronic Synapse Array. The device resistance for the processing was tuned one by one. The selection of the device is enabled by the multiplexer, followed by careful tuning of the device resistance by providing a stream of custom-made write/read pulses supplied by the Keithley 2450 source meter. Once the resistance tuning of the 36 devices was complete, the resistances were read out simultaneously using the same readout scheme as the photonic synapse array. The readout voltage in this case, supplied by the Keithley 2450 source meter, was 0.1 V instead of 0.5 V. The device was placed inside a metal box to reduce overall measurement noise, and the whole measurement was controlled by the LABVIEW program. See Figure S10b,c of Supporting Information for a schematic illustration.

■ ASSOCIATED CONTENT

SI Supporting Information

The Supporting Information is available free of charge at <https://pubs.acs.org/doi/10.1021/acsami.3c18719>.

Material reliability comparison of MAPbBr₃ NWs and thin-film in ambient condition; device lifetime test for MAPbBr₃ artificial synapses; retention and jitter of LTP conduction states in MAPbBr₃ thin-film Re-RAMs; photoresponse of control sample with semitransparent Au instead of ITO contacting the NWs; process flow of image contrast enhancement and pattern recognition in MAPbBr₃ NW-based artificial vision system; recognition accuracy study of the MAPbBr₃ NW-based artificial vision system with and without the presence of the photonic synapse as the preprocessing layer; response of MAPbBr₃ NW-based photonic synapse to variation in number of input light pulses; contrast enhancement demonstration in MAPbBr₃ NW-based photonic synapse; fabrication process flow of the MAPbBr₃ NW devices; and schematic illustrating the electrical measurement setups (PDF)

■ AUTHOR INFORMATION

Corresponding Author

Zhiyong Fan – Department of Electronic & Computer Engineering and Department of Chemical and Biological Engineering, The Hong Kong University of Science and Technology, Kowloon, Hong Kong SAR 999077, China; State Key Laboratory of Advanced Displays and Optoelectronics Technologies, HKUST, Kowloon, Hong Kong SAR 999077, China; Shanghai Artificial Intelligence Laboratory, Shanghai 200000, P. R. China; orcid.org/0000-0002-5397-0129; Email: eezfan@ust.hk

Authors

Swapnadeep Poddar – Department of Electronic & Computer Engineering, The Hong Kong University of Science and Technology, Kowloon, Hong Kong SAR 999077, China

Zhesi Chen – Department of Electronic & Computer Engineering, The Hong Kong University of Science and Technology, Kowloon, Hong Kong SAR 999077, China

Shivam Kumar – Department of Electronic & Computer Engineering, The Hong Kong University of Science and Technology, Kowloon, Hong Kong SAR 999077, China

Daquan Zhang – Department of Electronic & Computer Engineering, The Hong Kong University of Science and Technology, Kowloon, Hong Kong SAR 999077, China

Yucheng Ding – Department of Electronic & Computer Engineering, The Hong Kong University of Science and Technology, Kowloon, Hong Kong SAR 999077, China

Zhenghao Long – Department of Electronic & Computer Engineering, The Hong Kong University of Science and Technology, Kowloon, Hong Kong SAR 999077, China

Zichao Ma – Department of Electronic & Computer Engineering, The Hong Kong University of Science and Technology, Kowloon, Hong Kong SAR 999077, China; orcid.org/0000-0002-9868-4070

Qianpeng Zhang – Department of Electronic & Computer Engineering, The Hong Kong University of Science and Technology, Kowloon, Hong Kong SAR 999077, China

Complete contact information is available at:

<https://pubs.acs.org/doi/10.1021/acsami.3c18719>

Author Contributions

[†]S. Poddar and Z. Chen contributed equally to this work. The experiments were conceptualized and analyzed by Z. Fan and S. Poddar. S. Poddar was responsible for device fabrication, along with detailed structural and electrical characterizations and implementation of the artificial vision system. Z. Chen conducted the neural network simulations. Device fabrication and characterization were also assisted by S. Kumar, D. Zhang, Y. Ding, Z. Long, Z. Ma, and Q. Zhang. All authors contributed to manuscript writing and articulation.

Funding

Financial support for this work was provided by several sources, including the Hong Kong Research Grant Council's General Research Fund (Project nos. 16205321, 16309018, and 16214619), the Innovation Technology Commission Fund (Project no. GHP/014/19SZ), the HKUST Fund of Nanhai (grant no. FSNH-18FYTRI01), and the Shenzhen Science, Technology, and Innovation Commission (Project nos. JCYJ20180306174923335 and JCYJ20170818114107730).

Notes

The authors declare no competing financial interest.

■ ACKNOWLEDGMENTS

The authors also thank Dr. Roy Ho and Dr. Yuan Cai from the Material and Characterization Facility, The Hong Kong University of Science and Technology, for technical assistance with the TEM and FIB.

■ REFERENCES

- (1) Zhang, J.; Dai, S.; Zhao, Y.; Zhang, J.; Huang, J. Recent Progress in Photonic Synapses for Neuromorphic Systems. *Adv. Intell. Syst.* **2020**, *2*, 1900136.
- (2) Long, Z.; Qiu, X.; Chan, C. L. J.; Sun, Z.; Yuan, Z.; Poddar, S.; Zhang, Y.; Ding, Y.; Gu, L.; Zhou, Y.; Tang, W.; Srivastava, A. K.; et al. A Neuromorphic Bionic Eye with Filter-free Color Vision using Hemispherical Perovskite Nanowire Array Retina. *Nat. Commun.* **2023**, *14*, 1972.
- (3) Wang, Y.; Yin, L.; Huang, W.; Li, Y.; Huang, S.; Zhu, Y.; Yang, D.; Pi, X. Optoelectronic Synaptic Devices for Neuromorphic Computing. *Adv. Intell. Syst.* **2021**, *3*, 2000099.
- (4) Han, X.; Xu, Z.; Wu, W.; Liu, X.; Yan, P.; Pan, C. Recent Progress in Optoelectronic Synapses for Artificial Visual-perception System. *Small Struct.* **2020**, *1*, 2000029.
- (5) Chen, K.; Hu, H.; Song, I.; Gobeze, H. B.; Lee, W. J.; Abtahi, A.; Schanze, K. S.; Mei, J. Organic Optoelectronic Synapse Based on Photon-modulated Electrochemical Doping. *Nat. Photonics* **2023**, *17*, 629–637.

- (6) Zhou, F.; Zhou, Z.; Chen, J.; Choy, T. H.; Wang, J.; Zhang, N.; Lin, Z.; Yu, S.; Kang, J.; Wong, H. S. P.; Chai, Y. Optoelectronic Resistive Random Access Memory for Neuromorphic Vision Sensors. *Nat. Nanotechnol.* **2019**, *14*, 776–782.
- (7) Green, M. A. H. B.; Ho-Baillie, A.; Snaith, H. J. The Emergence of Perovskite Solar Cells. *Nat. Photonics* **2014**, *8*, 506–514.
- (8) Waleed, A.; Tavakoli, M. M.; Gu, L.; Wang, Z.; Zhang, D.; Manikandan, A.; Zhang, Q.; Zhang, R.; Chueh, Y.-L.; Fan, Z. Y. Lead-free Perovskite Nanowire Array Photodetectors with Drastically Improved Stability in Nanoengineering Templates. *Nano Lett.* **2017**, *17*, 523–530.
- (9) Gu, L.; Tavakoli, M. M.; Zhang, D.; Zhang, Q.; Waleed, A.; Xiao, Y.; Tsui, K. H.; Lin, Y.; Liao, L.; Wang, J.; et al. 3D Arrays of 1024-Pixel Image Sensors based on Lead Halide Perovskite Nanowires. *Adv. Mater.* **2016**, *28*, 9713–9721.
- (10) Waleed, A.; Fan, Z. Y. Fabrication of Stable Organometallic Halide Perovskite NWs based Optoelectronic Devices. *Sci. Bull.* **2017**, *62*, 645–647.
- (11) Waleed, A.; Tavakoli, M. M.; Gu, L.; Hussain, S.; Zhang, D.; Poddar, S.; Wang, Z.; Zhang, R.; Fan, Z. Y. All Inorganic Cesium Lead Iodide Perovskite Nanowires with Stabilized Cubic Phase at Room Temperature and Nanowire Array-based Photodetectors. *Nano Lett.* **2017**, *17*, 4951–4957.
- (12) Tavakoli, M. M.; Tsui, K.-H.; Zhang, Q.; He, J.; Yao, Y.; Li, D.; Fan, Z. Highly Efficient Flexible Perovskite Solar Cells with Antireflection and Self-cleaning Nanostructures. *ACS Nano* **2015**, *9*, 10287–10295.
- (13) Mei, A.; Li, X.; Liu, L.; Ku, Z.; Liu, T.; Rong, Y.; Xu, M.; Hu, M.; Chen, J.; Yang, Y.; et al. A Hole-conductor-free, Fully Printable Mesoscopic Perovskite Solar Cell with High Stability. *Science* **2014**, *345*, 295–298.
- (14) Cao, Y. B.; Zhang, D.; Zhang, Q.; Qiu, X.; Zhou, Y.; Poddar, S.; Fu, Y.; Zhu, Y.; Liao, J. F.; Shu, L.; Ren, B.; Ding, Y.; et al. High-efficiency, Flexible and Large-area Red/green/blue All-Inorganic Metal Halide Perovskite Quantum Wires-based Light-emitting Diodes. *Nat. Commun.* **2023**, *14*, 4611.
- (15) Ma, F.; Zhu, Y.; Xu, Z.; Liu, Y.; Zheng, X.; Ju, S.; Li, Q.; Ni, Z.; Hu, H.; Chai, Y.; Wu, C.; Kim, T. W.; Li, F. Optoelectronic Perovskite Synapses for Neuromorphic Computing. *Adv. Funct. Mater.* **2020**, *30*, 1908901.
- (16) Yang, L.; Singh, M.; Shen, S. W.; Chih, K. Y.; Liu, S. W.; Wu, C. I.; Chu, C. W.; Lin, H. W. Transparent and Flexible Inorganic Perovskite Photonic Artificial Synapses with Dual-Mode Operation. *Adv. Funct. Mater.* **2021**, *31*, 2008259.
- (17) Hao, D.; Zhang, J.; Dai, S.; Zhang, J.; Huang, J. Perovskite/organic Semiconductor-based Photonic Synaptic Transistor for Artificial Visual System. *ACS Appl. Mater. Interfaces* **2020**, *12*, 39487–39495.
- (18) Wang, Y.; Lv, Z.; Chen, J.; Wang, Z.; Zhou, Y.; Zhou, L.; Chen, X.; Han, S. T. Photonic Synapses Based on Inorganic Perovskite Quantum Dots for Neuromorphic Computing. *Adv. Mater.* **2018**, *30*, 1802883.
- (19) Eames, C.; Frost, J. M.; Barnes, P. R.; O’regan, B. C.; Walsh, A.; Islam, M. S. Ionic Transport in Hybrid Lead Iodide Perovskite Solar Cells. *Nat. Commun.* **2015**, *6*, 7497.
- (20) Xu, Z.; Liu, Z.; Huang, Y.; Zheng, G.; Chen, Q.; Zhou, H. To Probe the Performance of Perovskite Memory Devices: Defects Property and Hysteresis. *J. Mater. Chem. C* **2017**, *5*, 5810–5817.
- (21) Chen, S.; Huang, J. Recent Advances in Synaptic Devices Based on Halide Perovskite. *ACS Appl. Electron. Mater.* **2020**, *2*, 1815–1825.
- (22) Poddar, S.; Zhang, Y.; Gu, L.; Zhang, D.; Zhang, Q.; Yan, S.; Kam, M.; Zhang, S.; Song, Z.; Hu, W.; Liao, L.; Fan, Z. Y. Down-scalable and Ultra-fast Memristors with Ultra-High Density Three-dimensional Arrays of Perovskite Quantum wires. *Nano Lett.* **2021**, *21*, 5036–5044.
- (23) Zhang, Y.; Poddar, S.; Huang, H.; Gu, L.; Zhang, Q.; Zhou, Y.; Yan, S.; Zhang, S.; Song, Z.; Huang, B.; Shen, G.; Fan, Z. Y. Three-dimensional Perovskite Nanowire Array-based Ultrafast Resistive RAM with Ultralong Data Retention. *Sci. Adv.* **2021**, *7* (36), No. eabg3788.
- (24) Zhang, Q.; Zhang, D.; Gu, L.; Tsui, K. H.; Poddar, S.; Fu, Y.; Shu, L.; Fan, Z. Y. Three-Dimensional Perovskite Nanophotonic Wire Array-based Light-emitting Diodes with Significantly Improved Efficiency and Stability. *ACS Nano* **2020**, *14*, 1577–1585.
- (25) Gu, L.; Zhang, D.; Kam, M.; Zhang, Q.; Poddar, S.; Fu, Y.; Mo, X.; Fan, Z. Significantly Improved Black Phase Stability of FAPbI₃ Nanowires via Spatially Confined Vapor Phase Growth in Nanoporous Templates. *Nanoscale* **2018**, *10*, 15164–15172.
- (26) Xue, Z.; Xu, Y.; Jin, C.; Liang, Y.; Cai, Z.; Sun, J. Halide Perovskite Photoelectric Artificial Synapses: Materials, Devices, and applications. *Nanoscale* **2023**, *15*, 4653–4668.
- (27) Raifuku, I.; Chao, Y. P.; Chen, H. H.; Lin, C. F.; Lin, P. E.; Shih, L. C.; Chen, K. T.; Chen, J. Y.; Chen, J. S.; Chen, P. Halide perovskite for Low-power Consumption Neuromorphic Devices. *EcoMat* **2021**, *3*, No. e12142.
- (28) Han, T. H.; Tan, S.; Xue, J.; Meng, L.; Lee, J. W.; Yang, Y. Interface and Defect Engineering for Metal Halide Perovskite Optoelectronic Devices. *Adv. Mater.* **2019**, *31*, 1803515.
- (29) Srivastava, S.; Ranjan, S.; Yadav, L.; Sharma, T.; Choudhary, S.; Agarwal, D.; Singh, A.; Satapathi, S.; Gupta, R. K.; Garg, A.; Nalwa, K. S. Advanced Spectroscopic Techniques for Characterizing Defects in Perovskite Solar Cells. *Commun. Mater.* **2023**, *4*, 52.
- (30) Poddar, S.; Zhang, Y.; Chen, Z.; Ma, Z.; Fu, Y.; Ding, Y.; Chan, C. L. J.; Zhang, Q.; Zhang, D.; Song, Z.; Fan, Z. Image Processing with a Multi-Level Ultra-Fast Three Dimensionally Integrated Perovskite Nanowire Array. *Nanoscale Horiz.* **2022**, *7*, 759–769.
- (31) Chen, C.; Chen, Q.; Xu, J.; Koltun, V. Learning to See in the Dark. *Proceedings of the IEEE Conference on Computer Vision and Pattern Recognition*, 2018; pp 3291–3300.